論文 / 著書情報
Article / Book Information

Title	Backward analysis of U-bearing particles from the Fukushima Daiichi Nuclear Power Station using the Scheil–Gulliver solidification model of the U–Zr–Fe–O system
Authors	Ayumi Itoh, Masato Mizokami, Mutsumi Hirai
Citation	Journal of Nuclear Materials, vol. 614, ,
Pub. date	2025, 5
DOI	https://dx.doi.org/10.1016/j.jnucmat.2025.155892
Creative Commons	Information is in the article.

Journal of Nuclear Materials 614 (2025) 155892

Contents lists available at ScienceDirect

Journal of Nuclear Materials

journal homepage: www.elsevier.com/locate/jnucmat

Backward analysis of U-bearing particles from the Fukushima Daiichi Nuclear Power Station using the Scheil–Gulliver solidification model of the U–Zr–Fe–O system

Ayumi Itoh [a,*], Masato Mizokami [b], Mutsumi Hirai [b]

[a] Laboratory for Zero-Carbon Energy, Institute of Science Technology, 2-12-1, Ookayama, Meguro-ku, Tokyo 152-8550, Japan
[b] Tokyo Electric Power Company Holdings, Inc, 1-1-3 Uchisaiwai-cho, Chiyoda-ku, Tokyo 100-8560, Japan

HIGHLIGHTS

- Crystal structure and U–Zr–Fe ratio of U-bearing particle reflects debris state.
- Fe-addition promoted separation of solid solution to U-rich and U-depleted fluorite.
- Solid phases without Fe can be formed even from Fe-containing liquid states.
- U-bearing particles could originate from liquid above 1800 K during accidents.

ARTICLE INFO

Keywords:
U-bearing particle
Fukushima Daiichi Nuclear Power Station
Scheil–Gulliver
Backward estimation of fuel debris
Nearest-neighbor search

ABSTRACT

For the decommissioning of the Fukushima Daiichi Nuclear Power Station (FDNPS), a methodology is needed for evaluating the chemical conditions where fuel debris formed during the accident, which is also a starting point for estimating current in-vessel state. The crystal structures and compositions of fuel debris provide information about their formation mechanisms and solidification paths. In this study, we performed Scheil–Gulliver solidification simulation for a wide range of U–Zr–Fe–O compositions (1829 points), obtaining theoretical phase relations in the solidified state. Then, we developed a method of backward estimating possible liquid-state compositions and demonstrated this method on six samples taken from the FDNPS (so-called as "U-bearing particles") by comparing their morphologies and compositions with their theoretical counterparts in the solidified state. Results showed that all samples were likely formed from liquids with a wide range of oxygen to metals ratio from 0.14 to 1.70, and fluorite oxide without Fe could form even from Fe-containing compositions. Introducing Cr into the analysis with the U–Zr–Fe–Cr–O system is expected to improve this method, enabling the inclusion of Cr-rich spinel formation in the search conditions in future work.

1. Introduction

For the safe decommissioning of the Fukushima Daiichi Nuclear Power Station (FDNPS), its Primary Containment Vessels (PCV) have been inspected to evaluate the distributions and properties of the fuel debris. During PCV inspection, particulate materials containing uranium (U-bearing particles) were collected from deposits on survey equipment or sediment in the PCV, and analyses were performed to understand the properties of the fuel debris and help estimate the formation mechanism of the U-bearing particles.

Metallographic analyses of U-bearing particles were reported by Tokyo Electric Power Company [1] and the Japan Atomic Energy Agency [2,3]. These reports summarized analyses obtained via field-emission scanning electron microscopy (with wavelength-dispersive X-ray spectroscopy or Energy-Dispersive X-ray Spectroscopy [EDS]) and transmission electron microscopy of U-containing regions. A report published in 2021 presented measurements for particles obtained from Units 1 to 3, and a report in 2023 focused on particles from Unit 2. The morphology and elemental distribution of U-bearing particles were investigated using secondary electron images and characteristic X-ray mapping. Fluorite oxides, tetragonal oxides, and spinel structures were detected as major phases in many samples

* Corresponding author.
E-mail address: itoh.a.ae@m.titech.ac.jp (A. Itoh).

https://doi.org/10.1016/j.jnucmat.2025.155892
Received 9 January 2025; Received in revised form 5 May 2025; Accepted 12 May 2025
Available online 13 May 2025

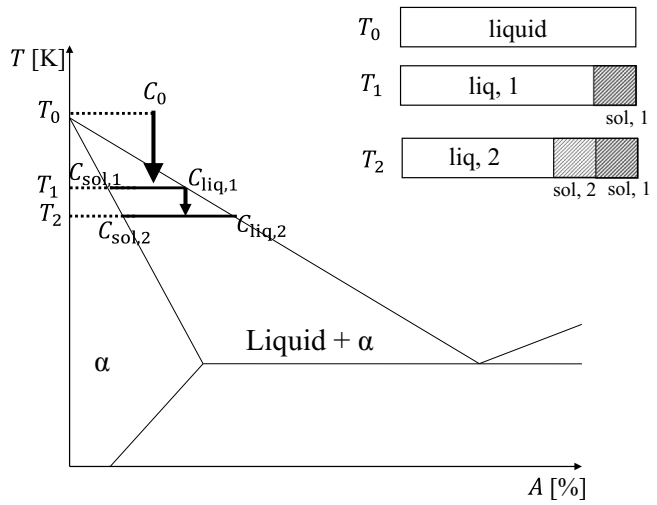

Fig. 1. Schematic illustration of the Scheil-Gulliver model solidification.

[4].

U-bearing particles are roughly classified into two categories: (1) particles formed by melting and solidification processes involving core materials (e.g. UO_2–Zr fuel cladding and Zr channel box) and structural materials (e.g. stainless steel [SS]) and (2) particles formed by evaporation and condensation. Because U-containing particles reflect the in-vessel condition during debris formation, their formation mechanism should be elucidated using metallographic analysis data to understand the properties of the fuel debris. Ohgi et al. [5] proposed four types of U-bearing particle formation mechanisms based on thermodynamic evaluation. They calculated pseudo-binary phase diagrams between UO_2–Zr–Fe and UO_2–ZrO_2–FeO in which the metallic atomic ratio (U:Zr:Fe) was obtained from EDS analysis results of U-bearing particles, classifying the possible phase relations in terms of temperature and O concentration. Their study contributes to the quantitative evaluation of debris formation. However, their method assumes that the metallic atomic ratio does not change during solidification, so it cannot handle cases involving phase separation, which causes changes in the metallic atomic ratio. Furthermore, the uncertainty of equilibrium calculation at low temperatures may not be small. Researchers should consider that solidification could occur in a nonequilibrium state, especially in the early stages of core degradation.

In the accident analysis of FDNPS, there have been works to improve materials interaction modelling in the severe accident (SA) code, which is based on the transport modelling coupling with thermodynamic calculation [6]. The accident scenarios were simulated by the MELCOR code, the results such as the mass amount of phase formed during core degradation were compared to the thermodynamic calculation using the inventory of materials (e.g. UO_2, Zr and ZrO_2) and temperature at the computation cell. The adjusted model parameters were validated by confirming that the simulation results agreed with the experimental works. This approach is a method of solving time evolution under given conditions (forward-in-time analysis), and requires assumptions and boundary conditions. What is compared to the fact from experiment is the consequence of calculation. However, in the analysis of FDNPS debris, there are still unknown in the accident progression, which means that the transport equations and boundary conditions cannot be exactly determined, and a method to estimate the formation pathways from the debris state (backward-in-time analysis) is necessary. The Scheil-Gulliver solidification model predicts the solidification behavior of alloys under more realistic, but non-equilibrium (eg. thermal gradient) conditions without time-dependent conditions; therefore, the model is instrumental in estimating the pre-solidification state of molten debris and useful to determine the boundary conditions of transport modelling approach.

In this study, we performed solidification simulations using the Scheil–Gulliver model for a wide range of U–Zr–Fe–O compositions (1829 points) using the Thermodynamics of Advanced Fuels–International Database (TAF-ID) [7] and investigated the correlation between the solidified phases and initial compositions of fuel debris. Then, we developed a method of backward-estimation of pre-solidification composition in the liquid state (composition candidates). Finally, this approach was applied to six U-bearing particles from the FDNPS.

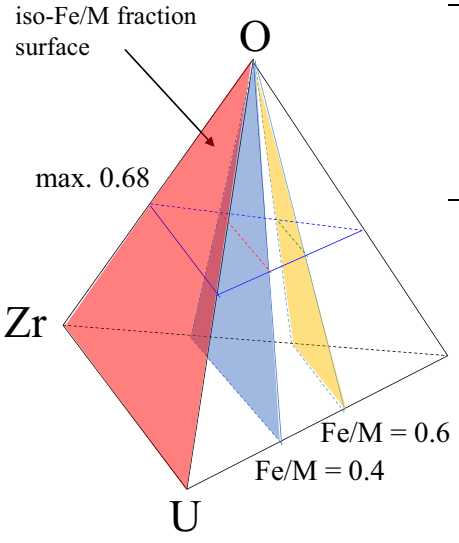

Fe/M	points	Fe/M	points
0	420	0.5	154
0.1	328	0.6	127
0.2	272	0.7	71
0.3	220	0.8	52
0.4	185		

total 1829 points

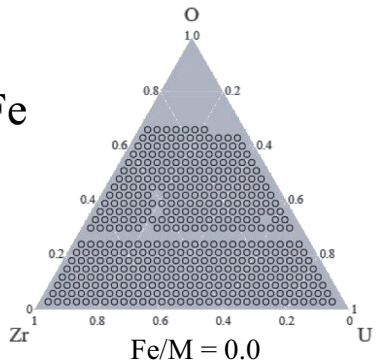

Fig. 2. Iso-Fe/M planes for sampling U–Zr–Fe–O compositions.

Table 1
Categorization of solid phases in the 1F sample.

Category	Phase name in TAF-ID	Space group	Thermodynamic model
ME	HCP_A3	$P6_3/mmc$ (No.194)	(Fe, U, Zr, Va) (O, Va)$_{0.5}$
	BCC_A2	Im $\bar{3}$ m (No.229)	(Fe, U, Zr, Va) (O, Va)$_3$
	FCC_A1	$Fm\bar{3}m$ (No.225)	(Fe, U, Zr, Va) (O, Va)
IM	C14_LAVES	$P6_3/mmc$ (No.194)	(Fe, Zr)$_2$(Fe, Zr, U)
	C15_LAVES	$Fd\bar{3}m$ (No.227)	(Fe, Zr)$_2$(Fe, Zr, U)
	FE3U3ZR4 (ε-phase)	–	$(Fe)_3(U)_3(Zr)_4$
	CHI_FEUZR (χ-phase)	–	$(Fe)_{50}(U)_{18}(Zr)_{32}$
MO2	C1_MO2	$Fm\bar{3}m$ (No.225)	(Fe^{2+}, Fe^{3+}, U^{3+}, U^{4+}, Zr^{2+}, Zr^{4+}, Va) (O^{2-}, Va)$_2$
ZRO2	ZRO2_TETR	$P4_2/nmc$	(Fe^{2+}, Fe^{3+}, U^{4+}, Zr^{4+}) (O^{2-}, Va)$_2$
FEOX	HALITE	$Fm\bar{3}m$ (No.225)	(Fe^{2+}, Fe^{3+}, U^{4+}, Zr^{4+}) (O^{2-}, Va)$_2$
	SPINEL	$Fd\bar{3}m$ (No.227)	(Fe^{2+}, Fe^{3+}, Zr^{4+}) (Fe^{2+}, Fe^{3+})$_2$ (Fe^{2+}, Va) (O^{2-})$_4$
	CORUNDUM	R3c (No.161)	(Fe^{2+}, Fe^{3+}, Zr^{3+}, Zr^{4+})$_2$ (Fe^{3+}, Va) (O^{2-})$_3$

(*) "Va" means vacancy.

2. Analysis procedure

2.1. Scheil–Gulliver solidification model

Under severe accident conditions, the core region of a nuclear power plant could have a temperature gradient in the axial and radial directions, leading to the quenching of molten materials during core degradation. In this case, the core melt can be suitably assumed to have solidified under restricted diffusion in the solid state; this differs from the assumption in equilibrium calculation, which is complete diffusion in both the liquid and solid states. The Scheil–Gulliver model, which was first presented by Gulliver in 1913 [8] and assumes infinitely fast diffusion in the liquid phase and zero or limited diffusion in the solid phase, is useful for this situation. Scheil formulated the differential equation and showed the analytical solution in 1942 [7]. Under these assumptions, the amount of solute swept during solidification equals the increase in solute in the liquid phase.

$$\left(C_{\mathrm{liq}} - C_{\mathrm{sol}}\right) d\phi_{\mathrm{sol}} = (1 - \phi_{\mathrm{sol}}) dC_{\mathrm{liq}}, \tag{1}$$

where C_{liq} and C_{sol} are the solute concentration at the solidification front in liquid and solids respectively, and ϕ_{sol} is the fraction of solids. With the partition coefficient $k = C_{\mathrm{sol}}/C_{\mathrm{liq}}$ and the initial concentration C_0, the analytical solution of Eq. (1) is obtained as follows:

$$C_{\mathrm{sol}} = kC_0(1 - \phi_{\mathrm{sol}})^{k-1}. \tag{2}$$

The partition coefficient k means the redistribution trend of the solute element. When k equals to 1, there will be no redistribution during solidification. If k is greater than 1, the solute will diffuse from the liquid to the solid. But if k is less than 1, the solute will diffuse from the solid to the liquid. As the special case, if $C_{\mathrm{liq}} \to 0$, it means that the solute in liquid will become zero and the solid-liquid partitioning calculation will be terminated as $C_{\mathrm{sol}} \to 0$ and $k \to 1$. This model was extended to multi-component system and is implemented by coupling it with a thermodynamic database, provided that the local equilibrium is realized at the liquid–solid interface. The solidification process is described as follows (Fig. 1):

(1) The liquid, with an initial concentration of C_0, is cooled to a temperature of T_1. The solid phase, with a concentration of $C_{\mathrm{sol},1}$, precipitates, and the concentration of the liquid becomes $C_{\mathrm{liq},1}$.
(2) As the temperature further drops to T_2, the concentration of the liquid becomes $C_{\mathrm{liq},2}$. A solid phase with a concentration of $C_{\mathrm{sol},2}$, equilibrating with the liquid, precipitates on the $C_{\mathrm{sol},1}$ solid phase because the solute in the solid phase cannot diffuse.
(3) This precipitation continuously occurs, causing the concentration distribution in the solid phase.

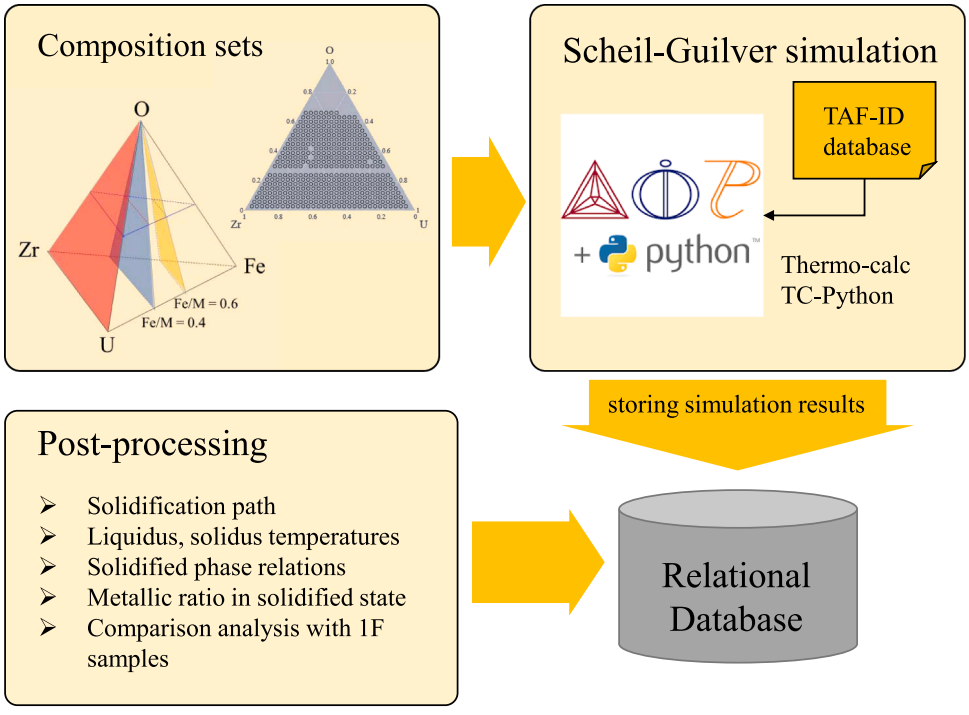

Fig. 3. Schematic illustration of software design for solidification analysis.

Table 2
1F sample list used for backward analysis in this study.

Reactor	Sample name	Region	Point	Normalized composition (at%)			Structure
				U	Zr	Fe + Cr	
Unit 1	1u-PCV-4-2017	15	1	8.1	80.3	11.6	tetragonal
			6	22.7	66.3	11.1	tetragonal
	1u-PCV-4-2017	22	1	55.8	42.8	1.4	cubic
			3	47.4	47.4	5.3	cubic
			4	48.1	48.1	3.8	cubic
			5	46.3	46.3	7.4	cubic
Unit 2	2u-PCVDEPO-4-2018	6	3	36.2	58.1	5.7	tetragonal
	2u-OPESHE-1-2014	30	4	50.5	30.6	18.9	cubic
	2u-OPESHE-1-2014	4	2	85.1	8.5	6.4	cubic
			4	76.1	16.7	7.3	cubic
Unit 3	3u-PCVDEPO-3-2018	5	1	53.5	27.7	18.8	cubic
			6	1.4	98.1	0.5	tetragonal

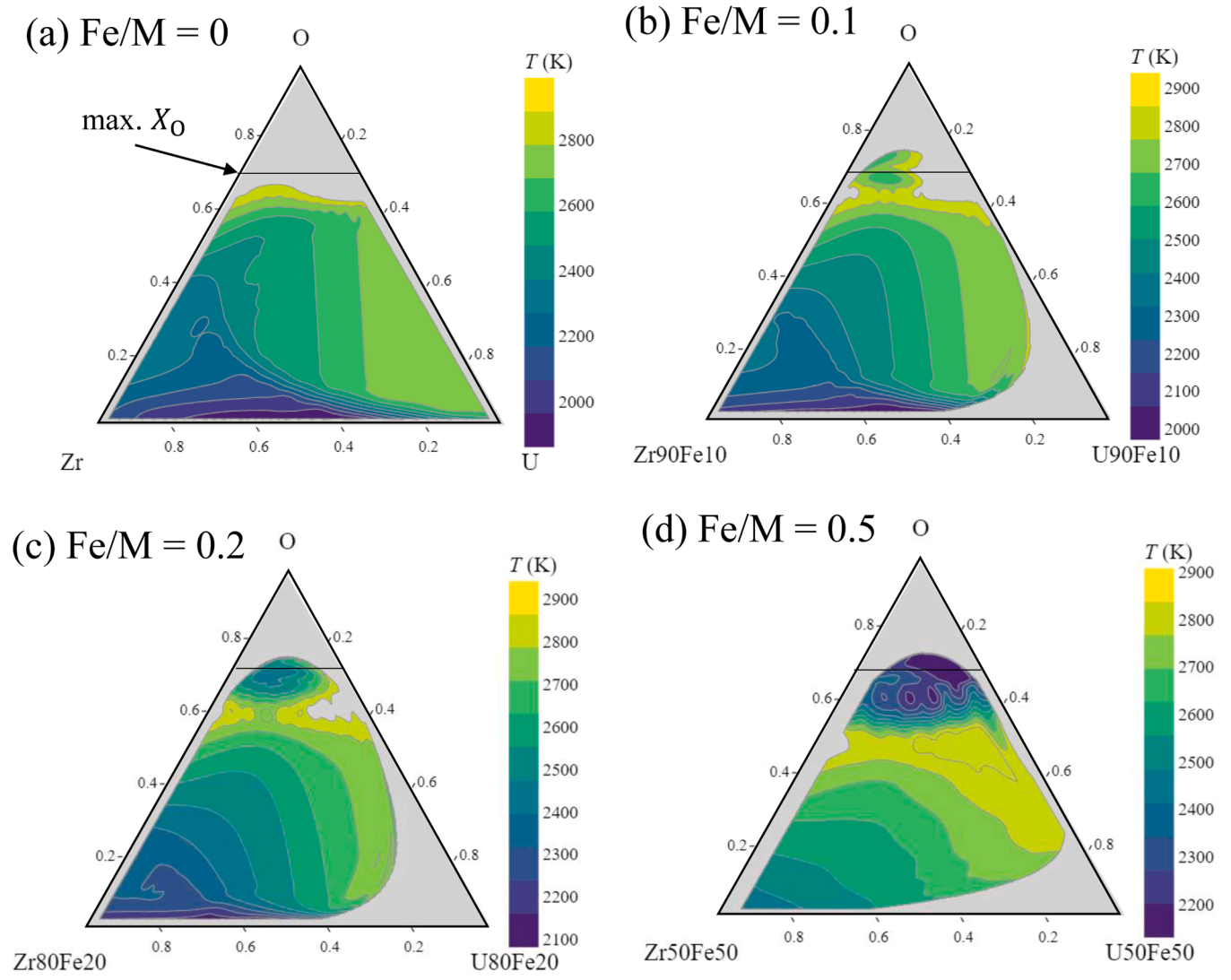

Fig. 4. Liquidus projection at (a) Fe/M = 0 (U–Zr–O), (b) Fe/M = 0.1, (c) Fe/M = 0.2 and (d) Fe/M = 0.5. The line at the O mole fraction of 0.68 marked as "max. X_O" in each ternary diagram indicates the maximum value to be calculated. The region above this maximum O fraction was drawn by extrapolation of the data points.

The software Thermo-Calc [9] provides four types of simulation models depending on how diffusion in the solid phase is handled. The "classic Scheil" model assumes that diffusion in the liquid phase is infinitely fast, diffusion in the solid phase is zero, and the liquid–solid interface is in equilibrium. This model approximates the solidification of many alloys well; however, the solidification of steels requires further treatment for "fast diffusers," or elements that diffuse infinitely fast in the solid phase, such as carbon in martensitic or diffusionless transformations [10]. The "Sheil with fast diffuser" model is used in this case. "Scheil with back diffusion" and "Scheil with solute trapping" are more advanced models designed for industrial applications, such as steel making and additive manufacturing. In this study, classic Scheil

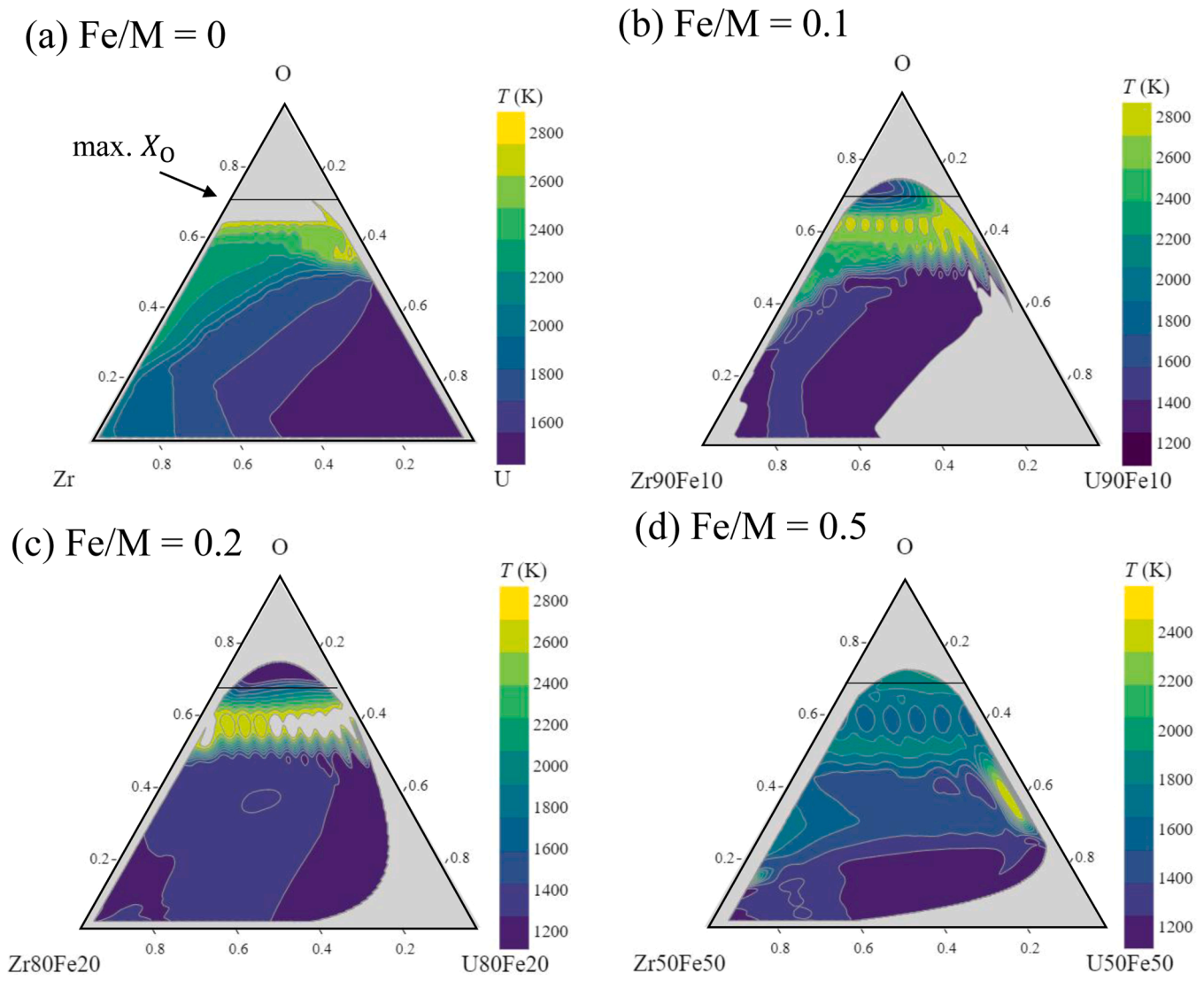

Fig. 5. Solidus projection (80 % solidified) at (a) Fe/M = 0 (U–Zr–O), (b) Fe/M = 0.1, (c) Fe/M = 0.2 and (d) Fe/M = 0.5. The line at the O mole fraction of 0.68 marked as "max. X_O" in each ternary diagram indicates the maximum value to be calculated. The region above this maximum O fraction was drawn by extrapolation of the data points.

simulation was used for solidification analysis. In the following sections, the Scheil-Gulliver calculation is using the "classic Scheil" module.

2.2. *U–Zr–Fe–O solidification analysis*

U–Zr–Fe–O compositions were selected from nine isosurfaces with Fe/(Fe + U + Zr) (Fe/M) values of 0, 0.1, 0.2, 0.3, 0.4, 0.5, 0.6, 0.7, and 0.8 (Fig. 2). The atomic fraction of O was selected from 0.03 to 0.68 at 0.03 increments, and the atomic fractions of U and Zr were taken from 0.03 to 0.99 at increments of 0.03. The total number of compositions used for the calculation were 1829. This composition range was determined to see an effect of Fe addition (from stainless steel) to the U–Zr–O system (from the fuel-cladding).

Calculation was performed using TC-Python [11], which is an add-on program of Thermo-Calc, with TAF-ID [7]. For each composition, the "classic Scheil" module was called with a maximum solidification fraction of 0.8 and a temperature step of 10 K. The numerical calculation for some compositions (especially at low O atomic fraction) failed to converge and was solved by limiting the maximum solidification fraction. At the beginning of one-point calculation, the liquidus temperature was searched and the precipitation from the liquid phase was calculated at each temperature down to the 80 % of the solidus temperature. The mole fraction and composition of the precipitated solid phase were evaluated at each temperature. When the temperature decreased from T_{n-1} to T_n (n is a calculation step), the equilibrium calculation was performed to the liquid phase at step *n-1* with T_n and then the solid phases were eliminated from the liquid state. Hence, the mole fraction of liquid phase, NL_n, was obtained as follows:

$$NL_n = NL_{n-1} - \sum_{j=1}^{J} NS_n(S_j) \tag{3}$$

where $NS_n(S_j)$ is the mole fraction of solid phase of S_j ($j = 1 \sim J$; J is the number of solid phases). Then, the solid-phase composition, mole fraction of element k in the solid phase of S_j as $X_n(S_j,\ k)$, was updated by dividing the accumulated volume fraction by the total moles at each temperature step as follows:

$$NS_n(S_j,\ k) = \sum_{i=1}^{n} \left[NS_{i-1}(S_j,\ k) + \left\{ NS_i(S_j) - NS_{i-1}(S_j) \right\} \cdot X_i(S_j,\ k) \right] \tag{4}$$

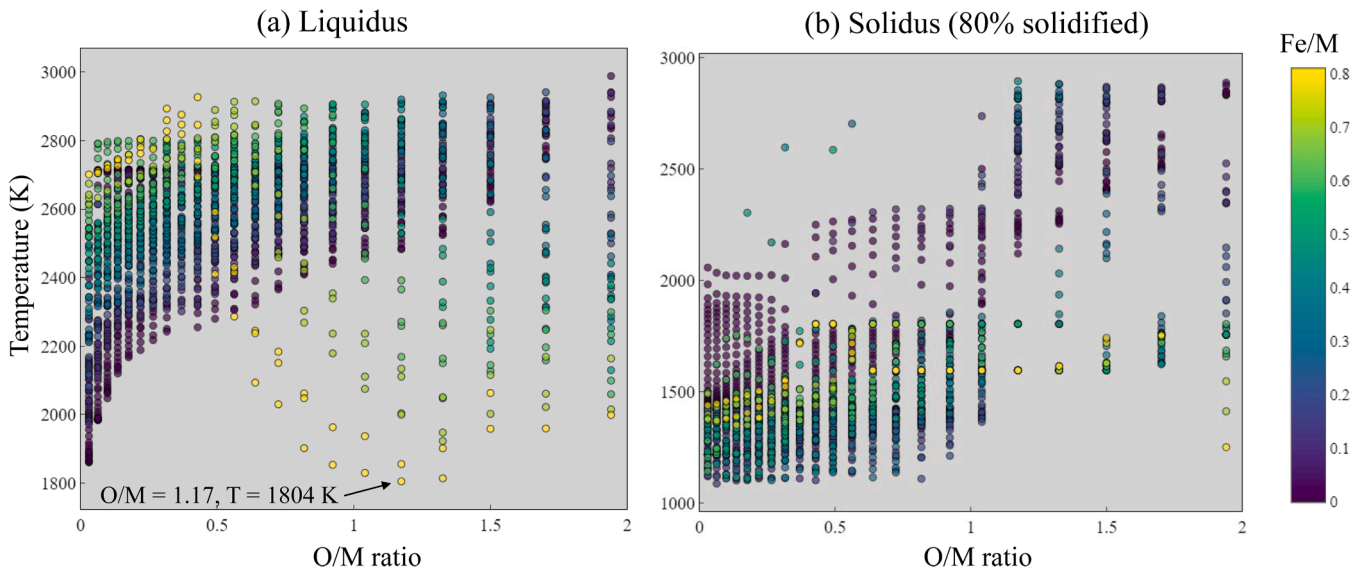

Fig. 6. Dependency of (a) liquidus and (b) solidus (80 % solidified) temperatures on O/M ratio.

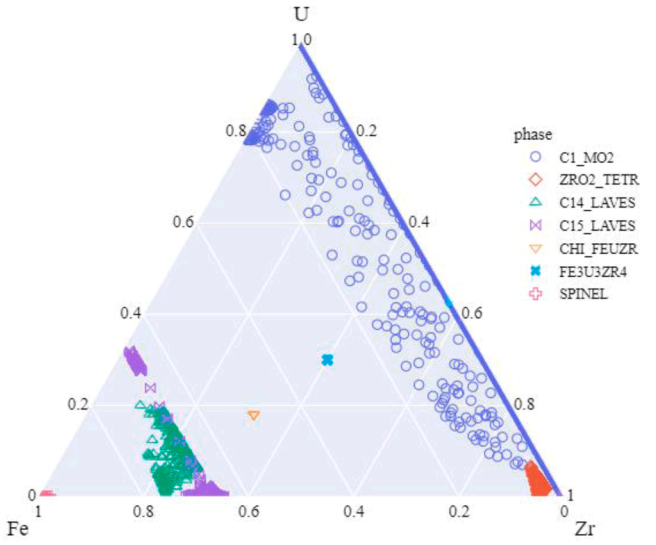

Fig. 7. Atomic ratio of metals in solidified phases identified in the 6 samples.

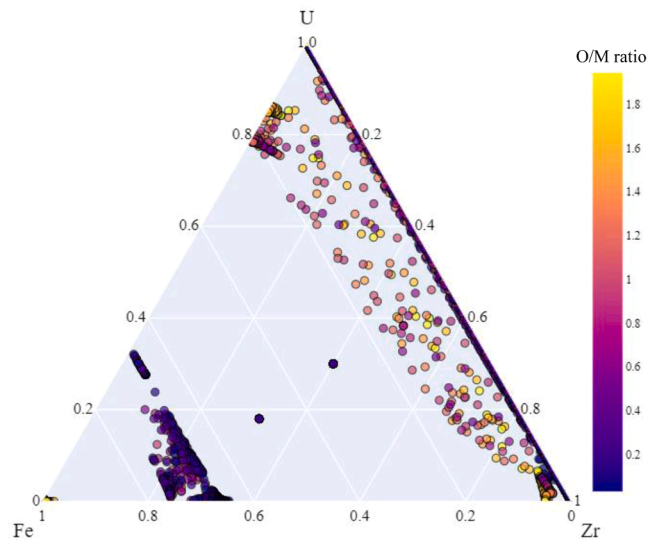

Fig. 8. Atomic ratio of metals in solidified phases identified by O/M ratio colors.

$$X(S_j,\ k) = \frac{NS_n(S_j,\ k)}{NS_n(S_j)} \tag{5}$$

where $N_i(S_j,\ k)$ is the moles of element k in the solid phase of S_j at the temperature step of i. The mole fraction of liquid phase, NL_n, and the composition of liquid phase, $X(L,\ k)$, was computed by eliminating the amount of solute distributed to the solid phase as follows.

$$X_n(L,\ k) = \frac{NL_{n-1}(k) - \sum_{j=1}^{J} NS_n(S_j,\ k)}{NL_n} \tag{6}$$

The calculated values (name of solid phase and atomic fractions of U, Zr, Fe, and O) at each temperature were stored in a relational database (see Fig. 2).

Python programs for postprocessing were developed to visualize the following information: (1) liquidus and solidus (80 % solidified) projections at Fe/M ratios of 0–0.8, (2) phase relations at temperatures with 80 % solidification fraction, (3) solid-phase atomic ratios in a U–Zr–Fe ternary diagram, and (4) comparison of U/(U + Zr) ratios between the liquid and fluorite solid. The many kinds of phases were calculated in the solidification analysis, which were grouped to improve readability according to Table 1. The metallic phases (HCP_A3, BCC_A2, and FCC_A1) and intermetallic phases (C14/C15_LAVES, ε-phase, and χ-phase Fe–Zr–U system) were categorized as ME and IM, respectively. Iron oxides (HALITE [wüstite], SPINEL [magnetite], and CORUNDUM [hematite]) were classified as FEOX. A schematic illustration of the analysis program is presented in Fig. 3.

2.3. Backward analysis via nearest-neighbor search algorithm

We used the EDS point analysis data of the U-bearing particles listed in Table 2, which shows the units where the samples were obtained (detailed locations were shown in the supplemental materials S1), the sample names, the estimated crystal structures, and the normalized metallic atomic ratios. In this study, the U-containing regions were chosen, which are mostly estimated as c-(U, Zr, Fe)O_2 (fluorite).

The Scheil–Gulliver calculation for a composition of $\boldsymbol{x} = (x_U,\ x_{Zr},\ x_{Fe},\ x_O)$ (x_i is the atomic fraction) yielded N datasets, each of which was

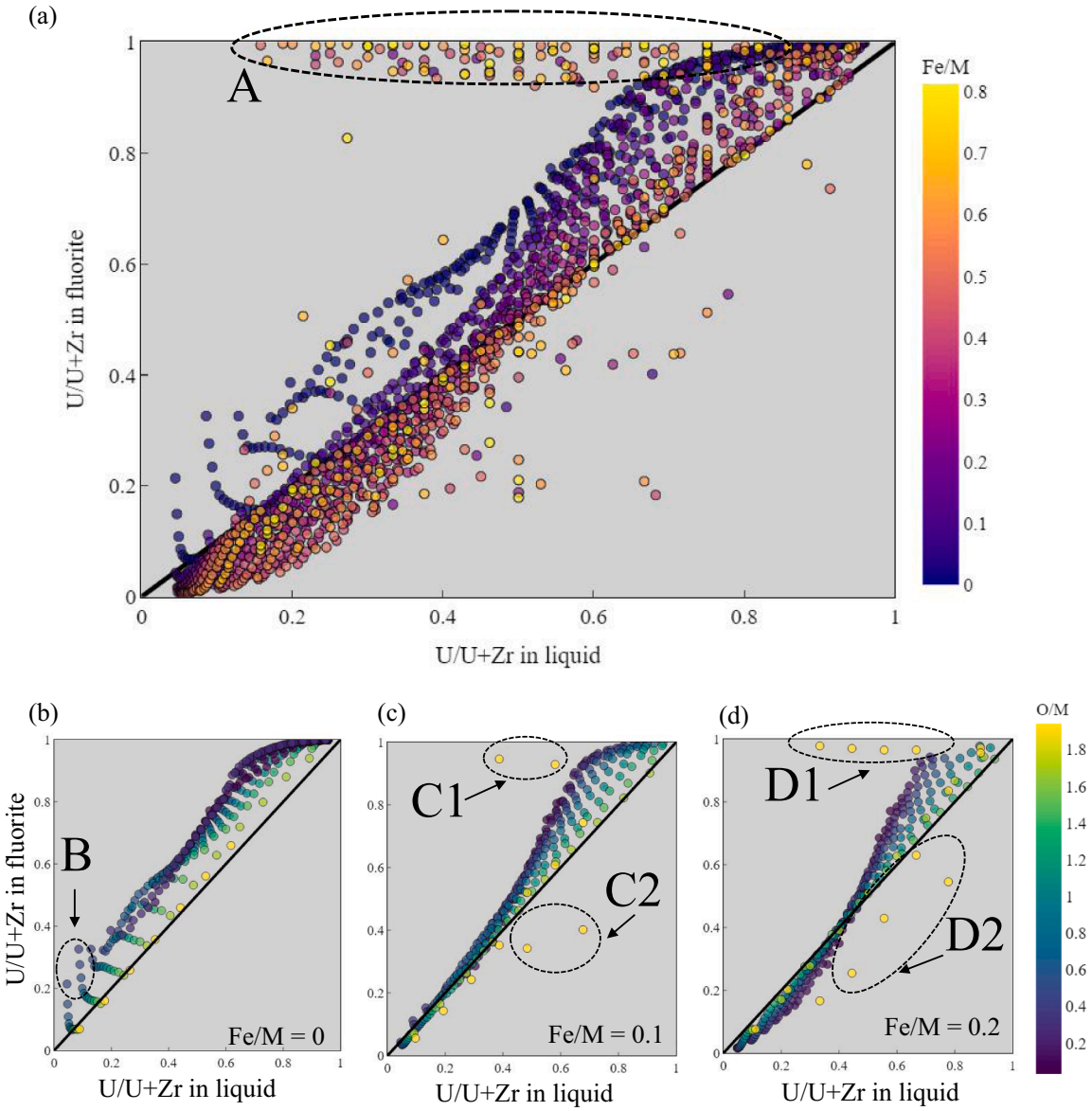

Fig. 9. Comparison of U/U+Zr in fluorite to initial composition, coloring with (a) Fe/M ratio, (b) O/M ratio with Fe/M of 0, (c) O/M ratio with Fe/M of 0.1 and (d) O/M ratio with Fe/M of 0.2. The solid line is diagonal connecting (0,0) and (1,1) indicating that the U/(U + Zr) ratios did not change during solidification. The data points marked by circle A were U-rich compounds when Fe was added to the system.

described as a phase ξ_i with a composition of $\boldsymbol{y_i} = (y^i_{\mathrm{U}}, y^i_{\mathrm{Zr}}, y^i_{\mathrm{Fe}}, y^i_{\mathrm{O}})$ ($i = 1 \sim N$). The composition of the U-bearing particle $\boldsymbol{X} = (X_{\mathrm{U}}, X_{\mathrm{Zr}}, X_{\mathrm{Fe}})$ was compared with the metallic atomic ratio in the solidified phase, which was derived as follows:

$$y^{*,i}_j = \frac{y^i_j}{1 - y^i_{\mathrm{O}}} \quad (j = \mathrm{U},\ \mathrm{Zr},\ \mathrm{Fe}). \tag{7}$$

The second norm of two different composition vectors between a U-bearing particle and any point composition $\boldsymbol{y^*_i} = (y^{*,i}_{\mathrm{U}}, y^{*,i}_{\mathrm{Zr}}, y^{*,i}_{\mathrm{Fe}})$ with the calculated solid phase was defined as follows:

$$d_i = \left[\left(x_{\mathrm{U}} - y^{*,i}_{\mathrm{U}}\right)^2 + \left(x_{\mathrm{Zr}} - y^{*,i}_{\mathrm{Zr}}\right)^2 + \left(x_{\mathrm{Fe}} - y^{*,i}_{\mathrm{Fe}}\right)^2 \right]^{0.5}. \tag{8}$$

The quantity described in Eq. (8) was used as an indicator of nearness to the target composition. In this study, the ten composition sets ($\boldsymbol{y^*}$) with the smallest distance were calculated with the constraints where the phase was fluorite (C1_MO2) or tetragonal zirconia (ZRO2_TETR). Then, composition candidates were obtained from $\boldsymbol{x} = (x_{\mathrm{U}}, x_{\mathrm{Zr}}, x_{\mathrm{Fe}}, x_{\mathrm{O}})$ most closely corresponding to $\boldsymbol{y^*}$.

3. Results

3.1. Liquidus and solidus temperatures

Figs. 4 and 5 show the liquidus and solidus projections, respectively, on the iso-surfaces with Fe/M values of 0, 0.1, 0.2, and 0.5. The line at the O mole fraction (X(O)) of 0.68 in each ternary diagram indicates the maximum value to be calculated. The region above this maximum O fraction was drawn to be extrapolated by the data points. In the case of Fe/M = 0, which was equivalent to the U–Zr–O system, the liquidus temperature increased with the O content and the iso-temperature line expanded to the U-rich region up to the O mole fraction of 0.4. When Fe was added to the U–Zr–O system, a low-liquidus-temperature region appeared in the oxygen-rich compositions. This tendency was evident in the high-Fe/M values, which was attributed to the eutectic reaction of the FeO–UO_2–ZrO_2 system. Similar characteristics were observed in the solidus temperature. Fig. 6 shows the dependence of these temperatures

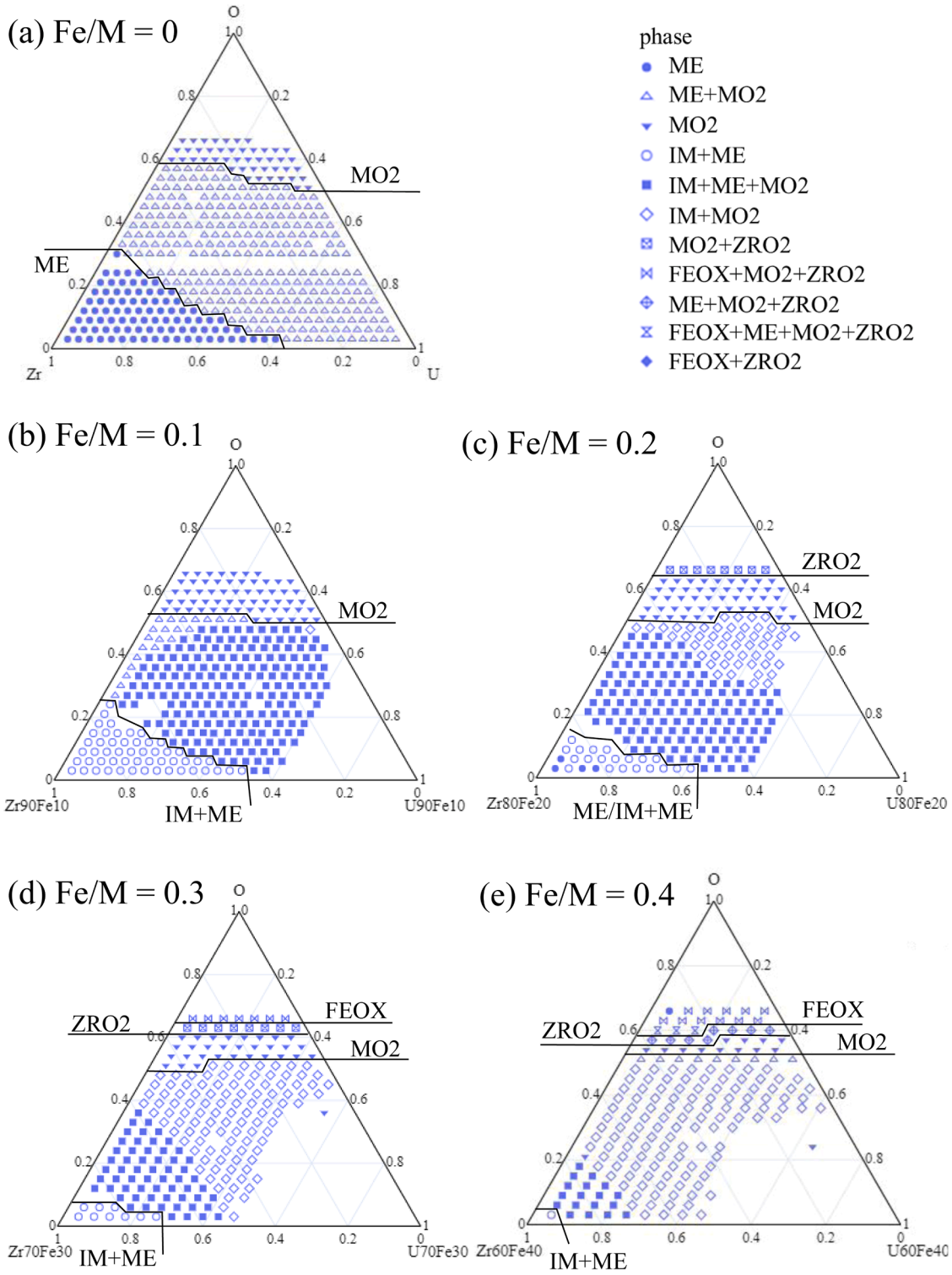

Fig. 10. Phase relations in 80 % solidified state with (a) Fe/M = 0 (U–Zr–O), (b) Fe/M = 0.1, (c) Fe/M = 0.2, (d) Fe/M = 0.3 and (e) Fe/M = 0.4.

on the O/M, defined as O/(U + Zr + Fe) in the system, and Fe/M ratios. At O/M ratios of below 0.5, Fe-addition increased the liquidus temperatures but decreased the solidus temperatures. Above the O/M ratio of 0.5, Fe-addition drastically decreased the liquidus temperatures, leading to a minimum value of 1804 K at the O/M value of 1.17.

3.2. Metallic atomic ratio distribution in solidified phases

Fig. 7 describes the atomic fractions of metals in the solidified phases, and Fig. 8 shows the O/M ratio of the U-Zr-Fe-O system corresponding to each point. The intermetallic compounds (C14/C15_LAVES, χ-phase, and ε-phase) appeared only at O/M ratios of less than 0.5, and fluorite (C1_MO2) had a wide range of U/(U + Zr) up to the Fe/M ratio of 0.2. By contrast, only small amounts of U and Fe could be dissolved in tetragonal zirconia (TETR_ZRO2), and Zr could only be slightly dissolved in spinel. Based on Fig. 8, these fluorite or tetragonal compounds could be formed from the liquid at a wide range of O/M ratios.

Fig. 9 shows the correlation between the U/(U + Zr) in the fluorite

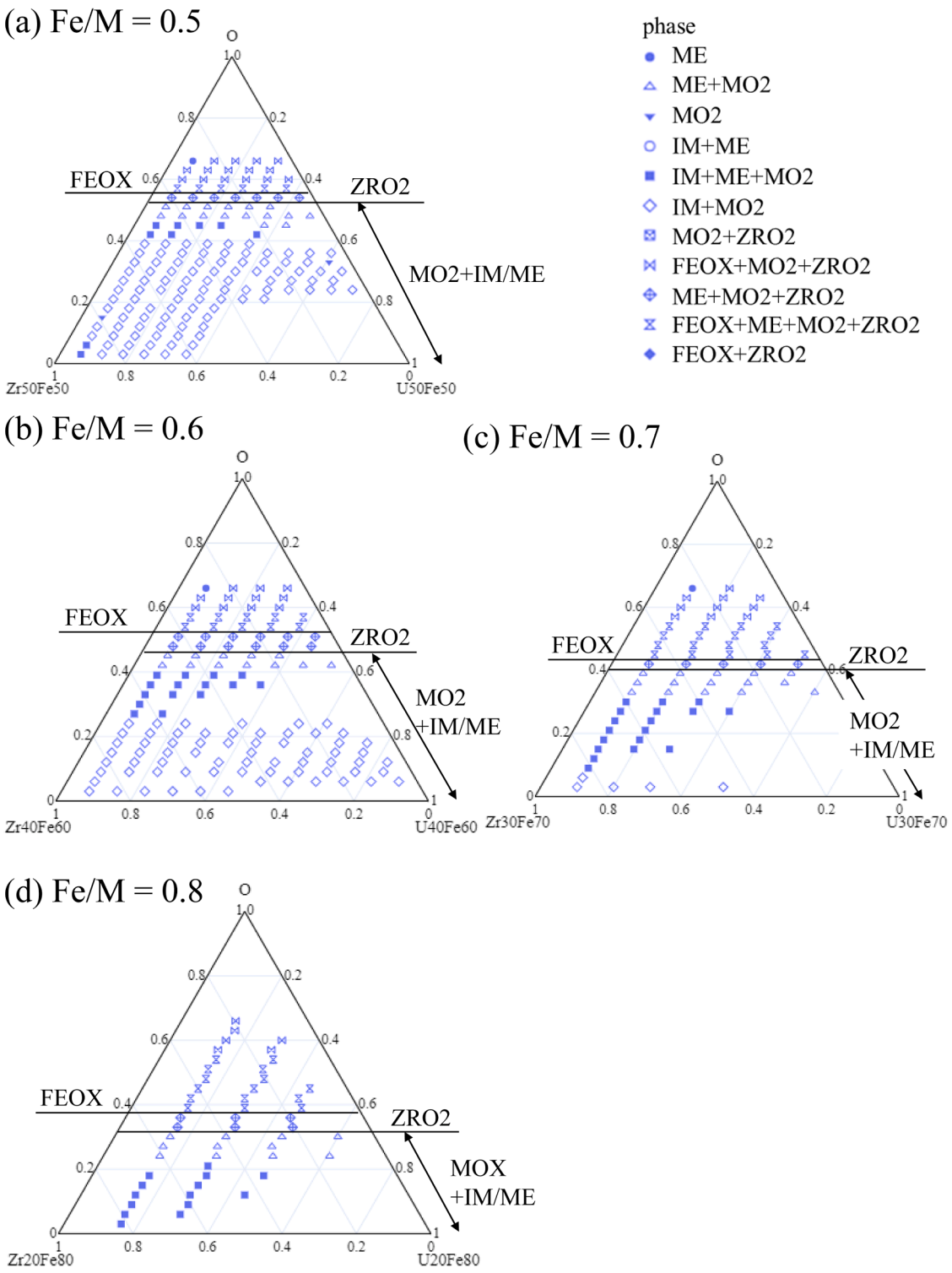

Fig. 11. Phase relations in 80 % solidified state with (a) Fe/M = 0.5, (b) Fe/M = 0.6, (c) Fe/M = 0.7 and (d) Fe/M = 0.8.

and the initial U/(U + Zr) coloring with the Fe/M ratio (Fig. 9(a)) and the O/M ratio (Fig. 9 (b–d)). The solid line on the figure is the diagonal line connecting (0,0) and (1,1) which indicates U/U + Zr ratios that did not change during solidification. The U/(U + Zr) ratios formed from the low-Fe/M-ratio compositions (dark purple points) shifted to U-rich compounds, whereas those formed from the high-Fe/M-ratio compositions (red, orange, and yellow points) separated into U-rich (encircled as A) and U-poor compounds. When the Fe/M ratio was zero and the O/M ratio was low, the coexistence of fluorite with α-Zr(O) resulted in the enrichment of U in the oxide (Area B in Fig. 9 (b)). As Fe was added to this state, the ε-phase (FE3U3ZR4), laves phase and BCC solid solution (U–Zr) were formed in addition to α-Zr(O). Formation of ε-phase and BCC solid solution reduced the U atomic fraction in fluorite, whereas formation of laves phase reduced the Zr atomic fraction in fluorite. In this study, volume fraction of ε-phase increased as the Fe/M ratio increased, which caused the decreased U/(U + Zr) in fluorite in the low U/(U + Zr) liquid (Fig. 9 (c) and (d)). With a large value of O/M ratio, the U/(U + Zr) of fluorite was almost on the diagonal line (Area B in

Table 3
Summary of phase relations at 80 % solidified state for various Fe/M ratios.

No.	Phase relations	Fe/M ratio								
		0.0	0.1	0.2	0.3	0.4	0.5	0.6	0.7	0.8
1	ME	X		X						
2	IM + ME		X	X	X	X				
3	IM + ME + MO2		X	X	X	X	X	X	X	X
4	IM + MO2		X	X	X	X	X	X	X	
5	ME + MO2	X	X			X	X	X	X	X
6	MO2	X	X	X	X	X	X			
7	MO2 + ZRO2			X	X					
8	ME + MO2 + ZRO2				X	X	X	X	X	X
9	FEOX + ME + MO2 + ZRO2					X	X	X	X	X
10	FEOX + MO2 + ZRO2					X	X	X	X	X

Fig. 9(b) Fe/M=0). Addition of Fe to this state caused the phase separation to the U-rich and Zr-rich oxides as the U/(U + Zr) in liquid state was increased (See areas C1 and C2 respectively in Fig. 9c and areas D1 and D2 in Fig. 9d).

3.3. Phase relations at 80 % solidified phases

Figs. 10 and 11 depict the phase relations in the 80 % solidified state on the iso-surfaces of Fe/M with the categories defined in Section 2.2. The minimum O level forming fluorite (MO2), tetragonal zirconia (ZRO2), and iron oxides (FEOX) and the maximum O level forming the metallic phases (ME and IM) are indicated as labeled lines in each figure. For Fe/M ratios under 0.5, the maximum O concentration at which the metallic phases (ME or IM+ME) formed, decreased with an increase in the Fe/M ratio. However, at the Fe/M ratios of 0.5 up to 0.8, metallic phases formed with fluorite (see Fig.11). Regarding the oxide compounds, the minimum O level forming fluorite (MO2) decreased with an increase in the Fe/M ratio and tetragonal zirconia (ZRO2) and iron oxides (FEOX) were only present in the range of Fe/M ratios from 0.2 to 0.3. Table 3 summarizes the phase relations of solidified state at each Fe/M ratio, showing the following characteristics:

(1) A two-phase region of fluorite and tetragonal zirconia formed at limited Fe/M ratios (0.2 and 0.3).
(2) Iron oxides could form along with other oxidic phases and a metallic melt at Fe/M ratios of 0.4 or above.
(3) A single phase of fluorite could form at Fe/M ratios of 0.5 or below.

3.4. Backward analysis results of 1F samples

Fig. 12 shows the composition candidates obtained from the nearest-neighbor search for each sample. The filled symbols denote the metal compositions obtained from the EDS measurement of the samples, and the analysis results are denoted by the unfilled symbols. For samples with multiple EDS points (Fig. 12 (a) 1u-PCV-4-2017#15, (b) 1u-PCV-4-2017#22, (e) 2u-OPESHE-1-2014#4, and 3u-PCVDEPO-3-2018#5, where # means region), areas with overlapping analysis results can be composition candidates, which are enclosed by black squares. The overlapping points (composition candidates) are summarized in Table 4. Regarding each sample with a single EDS measurement, ten points calculated through nearest-neighbor search are depicted in the figure. The data points marked with A – F are summarized in Table 4. Area A represents the highest Fe content or Fe/M ratios, and area F the lowest Fe content or lowest Fe/M ratios. The analysis results for each sample are as follows.

(a) 1u-PCV-4-2017#15

The overlapping points were obtained at the Fe/M ratios of 0.4 and 0.7 and had low U/U + Zr ratios (0.12–0.35). The O/M ratios at high-Fe/M values (area A) and low Fe/M values (area B) were in the range of 0.72–0.92 and 1.33–1.77, respectively.

(b) 1u-PCV-4-2017#22

The overlapping points were obtained in a wide range of Fe/M ratios (0.1–0.7) and had a narrow range of U/U + Zr ratios (0.44–0.55). The O/M ratios ranged from 0.37 to 1.17.

(c) 2u-PCVDEPO-4-2018#6

The candidates were obtained in a wide range of Fe/M ratios (0.1–0.8); their U/U + Zr ratios were within a narrow range and close to that of the sample. The O/M ratios for the ten candidates were in the range of 0.18–1.70.

(d) 2u-OPESHE-1-2014#30

Similar to the candidates for 2u-PCVDEPO-4-2018#6, the candidates for this sample were obtained in a wide range of Fe/M values (0.3–0.7); their U/U + Zr ratios were in a narrow range and close to that of the sample. However, their U/U + Zr ratios exhibited a scattered deviation from that of the sample. The O/M ratios for the ten candidates were in the range of 0.92–1.70.

(e) 2u-OPESHE-1-2014#4

The overlapping points were obtained at the Fe/M ratios of 0.5 and 0.7 and had high U/U + Zr ratios (0.79–0.90). The O/M ratios ranged from 0.32 to 0.92.

(f) 3u-PCVDEPO-3-2018#5

The overlapping points were obtained at the Fe/M ratios of 0.5 and 0.8 and had high U/U + Zr ratios (0.67–0.91). Their O/M ratios were in the range of 0.49–1.50.

4. Discussion

4.1. Outline of composition candidates obtained by backward analysis

Fig. 13 shows radar charts of the composition candidates for the 1F samples based on the data in Table 4. It shows the main variation occurs in Fe and O mole fractions compared to the U and Zr mole fractions. Specimen b) 1u-PCV-4-2017#22 is the exception where all 4 elements are equally variable. Given that a fully oxidic compound can be written as FeO–UO_2–ZrO_2, O mole fractions below 0.5 indicated an O-deficient hypo-oxide liquid state which is independent of the U, Zr and Fe atomic fraction. Hence, the samples could have either oxidic or hypo-oxidic liquid, affecting the liquidus temperatures and the interpretation of accident progression. Fig. 14 shows the liquidus temperatures of the composition candidates. Most samples remain relatively high at above 2500 K regardless of their oxidation (O/M ratio). By contrast, the values for 3u-PCVDEPO-3-2018#5 (triangle) scattered around 1800 K (Area A) and above 2600 K (Point B). The former case was caused by Fe-rich oxidic liquid, and the latter case was caused by Fe–(U, Zr)O_2 (metal and oxide) liquid. The variation of liquidus temperature with Fe/M ratio in this sample is also crucial for understanding formation mechanism of U-bearing particles because it reflects the extent of involvement of SS during debris formation.

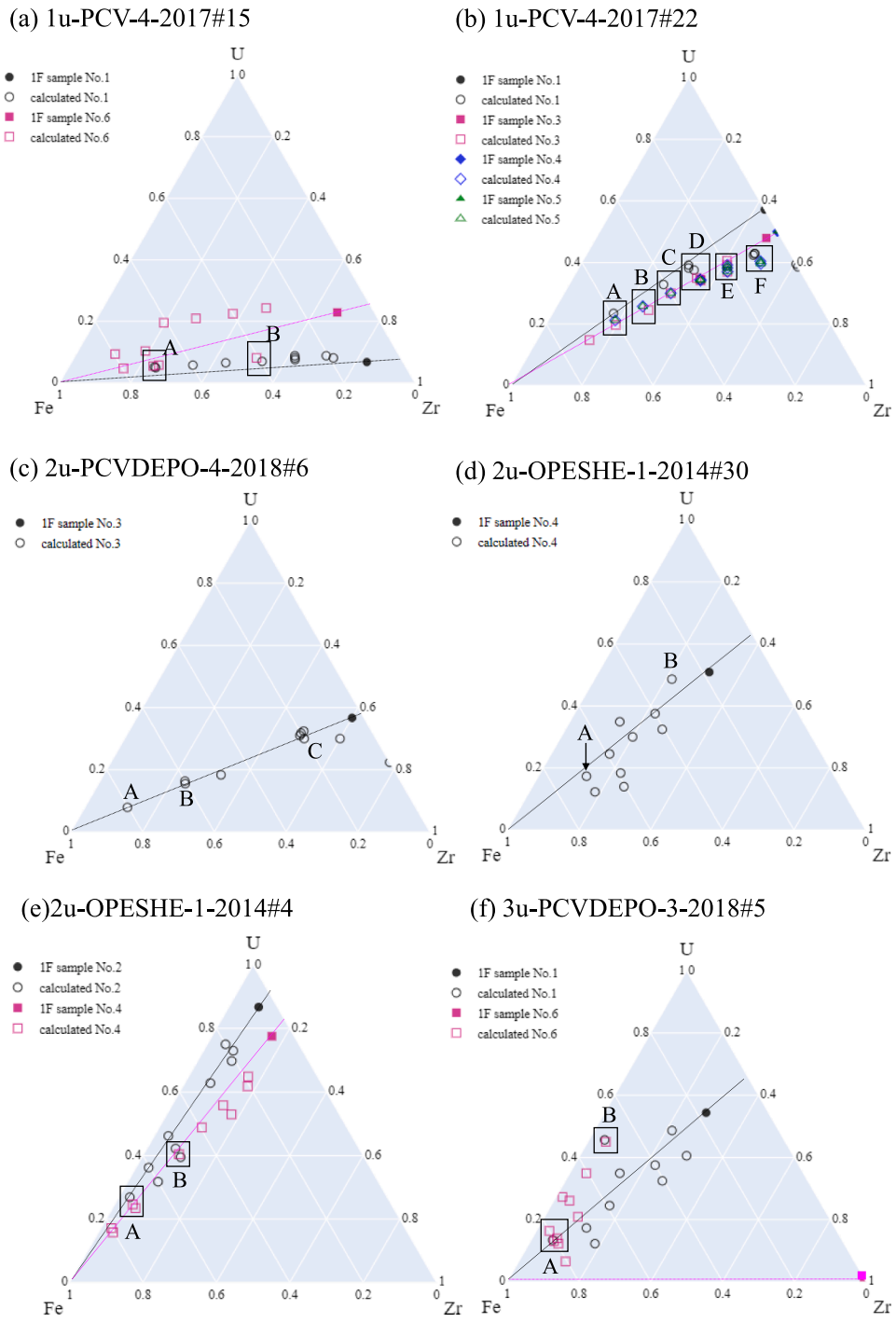

Fig. 12. Comparison of sample analyses and nearest neighbor calculations.

4.2. Detailed solidification paths of samples

We estimated the liquid-state composition of each sample using the nearest-neighbor search method and the composition in the solidified state obtained from the Scheil–Gulliver simulation. This section discusses the tendency of the composition candidates and the detailed solidification path of each sample. The solidification path is explained using temperature curves in terms of the solid fraction, and the composition change of the liquid phase during solidification are elucidated using points of the solidified phase relations. A figure is provided for each sample in Supplemental materials (S2).

The crystal structures observed in 1u-PCV-4-2017#15 and 2u-PCVDEPO-4-2018#6 were estimated as tetragonal phases (Table 2); however, the solubilities of U and Fe in these phases were too high to be reproduced via calculation in this study. This deviation could be explained by the metastable tetragonal phase of the UO_2–ZrO_2 system. Piluso et al. [12] observed a tetragonal solid solution in a sample from a VULCANO experiment [13] at a U/(U + Zr) value of approximately 0.4 and in a TMI-2 sample [14] at a U/(U + Zr) value of approximately 0.2. The formation of the metastable tetragonal phase was ascribed to the destabilization of the cubic phase at high temperatures. Because metastable phase formation is caused by nonequilibrium processes, it cannot be reproduced by thermodynamic simulation. Nevertheless, the cubic phase may need to be included in the search condition for a sample

Table 4
Composition candidates based on nearest-neighbor search by backward estimation.

Sample name	Region	Area (Fig. 12)	Initial composition (mole-fraction) and liquidus/solidus temperatures								
			ID	X_U	X_{Zr}	X_{Fe}	X_O	T_{liq} (K)	T_{sol} (K)	O/M	U/U+Zr
1u-PCV-4-2017	15	A	1745	0.03	0.14	0.41	0.42	2580	1804	0.72	0.18
			1746	0.06	0.11	0.41	0.42	2475	1804	0.72	0.35
			1750	0.03	0.13	0.39	0.45	2421	1595	0.82	0.19
			1755	0.03	0.13	0.36	0.48	2354	1595	0.92	0.19
		B	1399	0.03	0.23	0.17	0.57	2773	1804	1.33	0.12
			1414	0.03	0.19	0.15	0.63	2476	1685	1.70	0.14
1u-PCV-4-2017	22	A	1656	0.15	0.11	0.38	0.36	2798	1380	0.56	0.58
			1660	0.12	0.12	0.37	0.39	2812	1469	0.64	0.50
		B	1548	0.12	0.13	0.24	0.51	2809	1803	1.04	0.48
			1496	0.18	0.17	0.35	0.30	2687	1459	0.43	0.51
		C	1336	0.21	0.17	0.26	0.36	2691	1362	0.56	0.55
			1318	0.21	0.21	0.28	0.3	2636	1160	0.43	0.50
		D	1213	0.15	0.15	0.13	0.57	2850	2817	1.33	0.50
			1149	0.21	0.22	0.18	0.39	2625	1299	0.64	0.49
			1060	0.3	0.32	0.26	0.12	2542	1299	0.14	0.48
		E	868	0.27	0.31	0.15	0.27	2533	1396	0.37	0.47
			978	0.18	0.19	0.09	0.54	2710	2602	1.17	0.49
			942	0.21	0.23	0.11	0.45	2606	1376	0.82	0.48
		F	579	0.3	0.33	0.07	0.30	2528	1335	0.43	0.48
			674	0.21	0.26	0.05	0.48	2555	1419	0.92	0.45
2u-PCVDEPO-4-2018	6	A	1793	0.06	0.09	0.61	0.24	2805	1553	0.32	0.40
		B	1670	0.09	0.13	0.33	0.45	2773	1803	0.82	0.41
		C	997	0.12	0.2	0.08	0.6	2814	2795	1.50	0.38
2u-OPESHE-1-2014	30	A	1757	0.09	0.07	0.36	0.48	2179	1595	0.92	0.56
		B	1231	0.18	0.08	0.11	0.63	2656	1785	1.70	0.69
2u-OPESHE-1-2014	4	A	1734	0.18	0.02	0.47	0.33	2890	1453	0.49	0.90
			1744	0.15	0.03	0.43	0.39	2915	1803	0.64	0.83
		B	1520	0.27	0.05	0.32	0.36	2808	1428	0.56	0.84
			1478	0.30	0.08	0.38	0.24	2771	1278	0.32	0.79
			1543	0.21	0.05	0.26	0.48	2904	1688	0.92	0.81
3u-PCVDEPO-3-2018	5	A	1805	0.09	0.04	0.54	0.33	2591	1803	0.49	0.69
			1823	0.06	0.03	0.37	0.54	1804	1595	1.17	0.67
			1825	0.06	0.03	0.34	0.57	1813	1613	1.33	0.67
			1821	0.06	0.04	0.39	0.51	1829	1595	1.04	0.60
		B	1557	0.21	0.02	0.23	0.54	2863	1804	1.17	0.91
			1569	0.18	0.02	0.20	0.60	2428	1595	1.50	0.90

having a tetragonal phase with a high U/(U + Zr) ratio.

By including the cubic phase in the search condition for 1u-PCV-4-2017#15, we obtained reasonable candidates. The solidification path for 1u-PCV-4-2017#15 is shown in S1.1 (Supplemental material 1: S1), labeled calculation numbers (nos.) 1750 and 1414. The composition of no. 1414 had more O but less Fe than that of no. 1750. Both paths showed similar liquidus and solidus temperatures (S1.1(a)). The solidified phases of no. 1414 included SPINEL, whereas those of no. 1750 included HALITE and BCC_A2. The analysis result of no.1414 was consistent with the report [2] identifying tetragonal and spinel phases in this sample. The inclusion of Cr in the calculation was expected to expand the spinel-forming region, as discussed in Section 4.3.

The solidification path for 1u-PCV-4-2017#22 is shown in S1.2, labeled nos. 1149 and 1618, with no. 1149 having more oxygen but a lower Fe atomic fraction. The solidified state in both cases included intermetallic compounds (C14_LAVES, C15_LAVES, and FE3U3ZR4), and C1_MO2 did not have Fe. The Fe content of this sample was almost negligible, confirming that fluorite without Fe can also form from Fe-containing compositions. Therefore, the low Fe atomic fraction in the sample does not deny the possibility that this particle was formed by a reaction with SS.

The solidification path for 2u-PCVDEPO-4-2018#6 is shown in S1.3, labeled nos. 1663 and 1793, with no. 1663 having more O but a lower Fe atomic fraction. Although they had similar solidification paths, with solidified states of C1_MO2 and BCC_A2, the solid fraction in no. 1663 was more sensitive to temperature. The crystal structure of this sample was estimated as a tetragonal phase, but we added a cubic phase in the search condition for the same reason as for 1u-PCV-4-2017#15.

The solidification path for 2u-OPESHE-1-2014#30 is shown in S1.4. We selected nos. 1231 and 1757 to demonstrate that solid solutions with similar compositions can form despite having widely different Fe/M ratios. The liquidus temperature in no. 1757 was lower than that in no. 1231 because of the FeO–UO_2–ZrO_2 eutectic reaction. Solidification path no. 1231 showed phase separation to C1_MO2 and ZRO2_TETR, whereas HALITE and BCC_A2 additionally separated in no. 1757. This sample showed fluorite and spinel, indicating that no. 1757 was similar to the sample.

The solidification path for 2u-OPESHE-1-2014#4 is shown in S1.5, labeled nos. 1544 and 1734, with no. 1544 having more O but less Fe. The solidification path in both cases was similar, separated into C1_MO2 and BCC_A2. This result differed from the sample result, which showed fluorite and spinel. This point was improved by introducing Cr in the simulation, as explained in Section 4.3.

The solidification path for 3u-PCVDEPO-3-2018#5 is shown in S1.6, labeled nos. 1557 and 1805, with no. 1557 having more O and U but a lower Fe atomic fraction. The oxidic liquid of no. 1557 was separated into C1_MO2 and ZRO2_TETR. For no. 1805, the metals above the solubility limit of the dioxides formed as BCC_A2 in addition to C1_MO2 and ZRO2_TETR. Because this sample had U-rich fluorite and Zr-rich tetragonal phases without metals, no. 1557 was considered to be more similar to the sample.

According to the report validating TAF-ID with the experimental work simulating ex-vessel corium (U–Zr–Fe–Si–Ca–O) [15], thermodynamic calculation well agreed with the experimental results for the UO_2-corium, especially for liquidus and solidus temperatures and composition of phases. However, the U/(U+Zr) ratio in the fluorite deviated from the experimental result when there had miscibility gap at high temperature. This deviation may affect the analysis result of 2u-OPESHE-1-2014#30 and 3u-PCVDEPO-3-2018#5 because their candidates have two fluorite phases. It is expected that the accuracy of

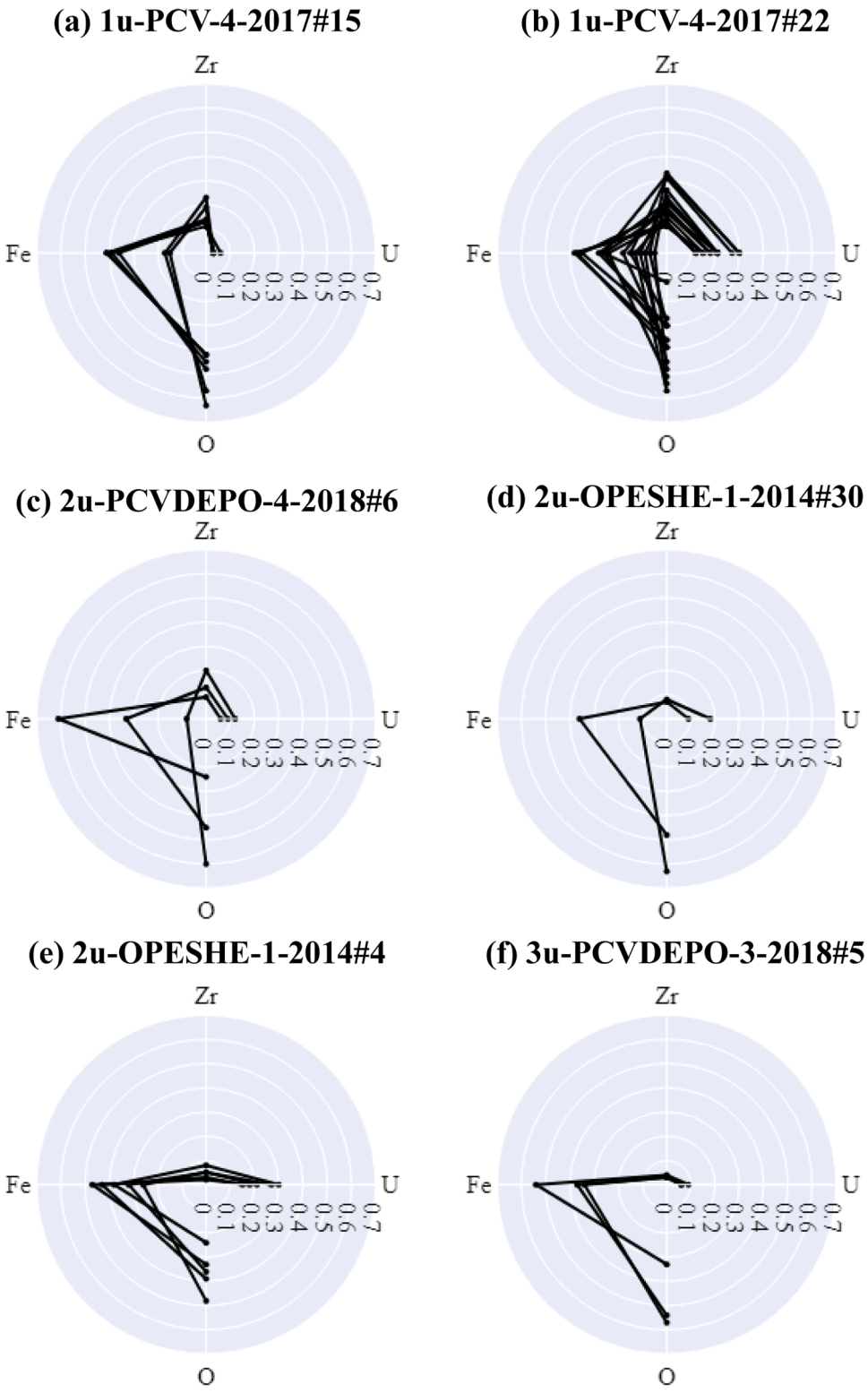

Fig. 13. Composition candidates obtained by nearest-neighbor search displayed on the radar charts of mole fraction for the 4 main elements of the nearest neighbors identified in Fig. 12.

prediction in this study will be improved by the further refinement of database.

4.3. *Influence of Cr on solidification analysis*

In this study, we calculated solidified phases in the U–Zr–Fe–O system while regarding Fe as Fe + Cr and compared the results with the obtained sample compositions. Although we obtained consistent results in most cases, the analysis for 2u-OPESHE-1-2014#4 showed inconsistency in spinel formation. This was because of the limited SPINEL (Fe_3O_4) formation in the U–Zr–Fe–O system. Because the FDNPS samples showed the coexistence of Cr-rich spinel with fluorite, the influence

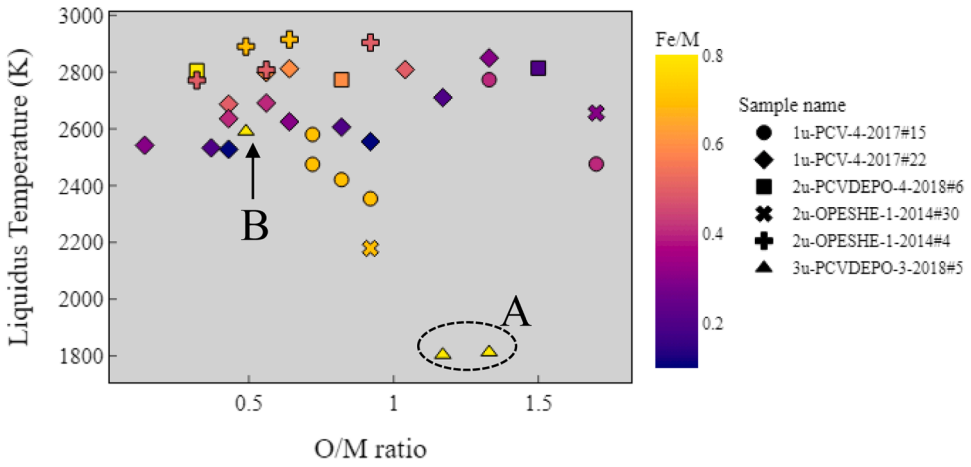

Fig. 14. Liquidus temperatures of nearest neighbor composition candidates.

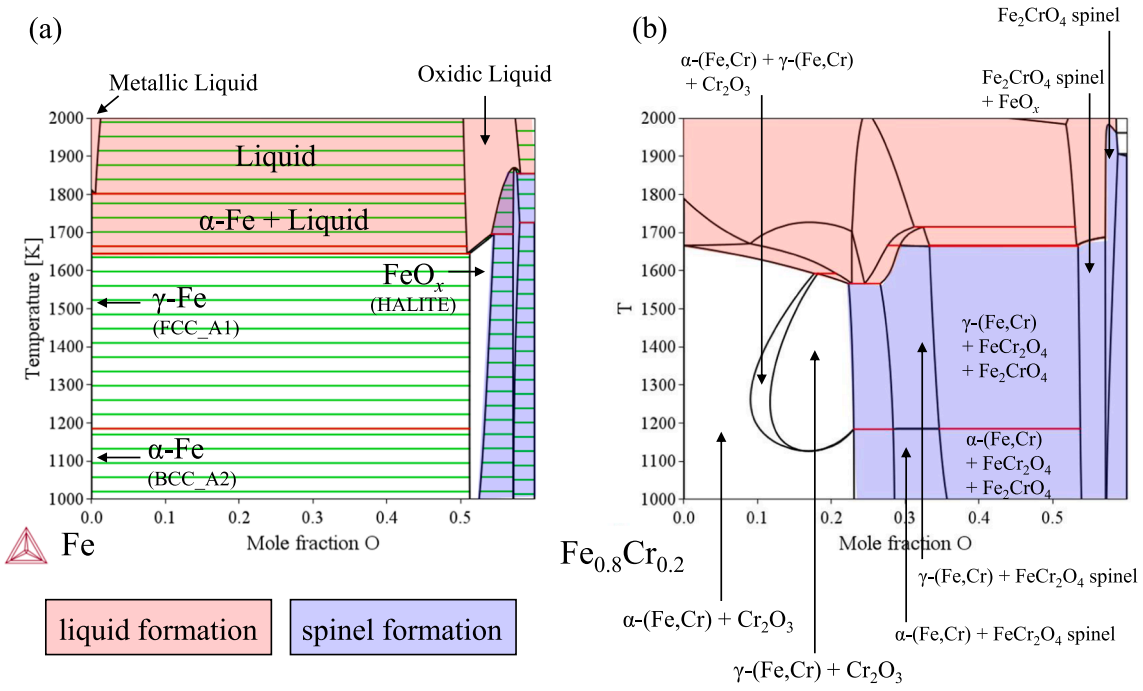

Fig. 15. Difference in spinel formation range with (a) Fe–O system and (b) $Fe_{0.8}Cr_{0.2}$–O system.

of Cr on the U–Zr–Fe–O system should be considered. For a lower computation cost of U–Zr–Fe–Cr–O system simulation, using a constant ratio of Fe/Cr that is equivalent to that of nuclear stainless steel (i.e. AISI 316) is reasonable. Fig. 15 is a comparison of binary phase diagrams of Fe–O and $Fe_{0.8}Cr_{0.2}$–O, highlighting how Cr inclusion affected the phase formation results. The blue and red areas indicate the spinel and liquid formation ranges, respectively. Compared with that of the Fe–O system, the spinel formation area here was much wider, and Cr_2O_3 was seen from an oxygen content of about 0.1 mole. Therefore, Fe/Cr-rich spinel (Fe_2CrO_4, $FeCr_2O_4$) or chromium oxides (Cr_2O_3) may appear in areas with metallic (ME) and intermetallic compounds (IM) in U–Zr–Fe–O system simulation, enabling the inclusion of Cr-rich spinel in the search condition. This improvement is expected in future work.

4.4. Inclusion of other elements to the U–Zr–Fe–O system

It would be worthwhile to discuss other elements to be included in the U–Zr–Fe–O system for future work. Candidate elements are the stainless-steel components (Cr and Ni), neutron absorber (B and C) and fission products (FPs). As for the stainless-steel components, the inclusion of Cr is necessary as shown in the previous section. Additionally, the inclusion of Ni would be effective in evaluating the melting reaction under reducing condition between the fuel debris and stainless steel or nickel alloy due to the chemical affinity of the Zr–Ni–Fe system. However, since the Zr–Ni–Fe system of TAF-ID has been validated mainly for experimental results below 1473 K, the addition of Ni may affect the prediction accuracy of the liquidus temperatures of system. Therefore, it is recommended to include Ni only for a specific purpose, such as to investigate segregation in Ni-enriched regions. Second, boron and carbon from the neutron absorber react with Fe and Zr to form borides and carbides, which affect the mechanical properties of fuel debris [16]. Meanwhile, the amount of these elements that evaporated during the fuel debris formation process is considered to be not small, because B_4C and control rod-derived debris may have reacted with high-temperature steam to release boric acid gas [17,18]. Finally, inclusion of FPs is discussed. The fission gases and volatile elements do not need to be

included in the solidification process. Excluding the evaporated elements, FPs can be categorized as (1) elements dissolved in the fuel matrix (rare earth, Zr, Nb and Mo), (2) elements forming oxide precipitates (Ba, Sr and Zr) and (3) elements forming metallic precipitates (Ru, Tc, Rh, Pd and Mo) [19]. Elements in category 1 may affect the solubility of cation atoms in the fluorite matrix, elements in category 2 may form perovskite-type compounds with U and Zr, and category 3 may react with Ni and Zr in a reducing atmosphere. Regarding Mo, the chemical form depends on the oxygen partial pressure (Mo or MoO_2), which becomes an indicator obtaining information about the oxygen potential in the fuel. The importance of these elements depends on the amount of material evolution during the core degradation. The approximate weight of FPs elements at the time of core degradation of Unit 2 was obtained by summing up the radionuclides at 3 days after the accident [20] as follows: (1) rare earth, Nb and Mo; 900 kg, (2) Ba and Sr; 150 kg and (3) Ru, Tc, Rh, Pd and Mo; 500 kg. The weight of each category is less than 1 % of the UO_2 inventory (approx. 103.3 tons); therefore, these elements basically do not need to be included in the solidification analysis. However, samples of Ni sulfides with scattered platinum group FPs were found in Unit 2 [3], and the formation mechanism may help to understand the in-core conditions. For FPs elements, it is recommended to include relevant elements in the analysis depending on the situation and purpose.

5. Conclusion

This study investigates the development of a method of backward estimation of the state of FDNPS debris via Scheil–Gulliver solidification analysis for a U–Zr–Fe–O system. It is based on the idea that (1) the 1F sample composition may reflect the state at the time of solidification of particles and (2) the composition at the time of melting can be determined by comparing the backward estimates with the sample composition. The developed method was applied to six U-bearing particles, and liquid-state composition candidates were proposed. Consistent phase relations and compositions were obtained from five samples by adding a cubic structure to the search condition of samples with tetragonal structures. However, the coexistence of spinel with fluorite was not reproduced in one sample due to the absence of Cr-rich spinel phase calculation. Introducing U–Zr–(Fe, Cr)–O simulation is expected to improve this method in future work. The improved estimation of the debris composition and their local conditions of formation in each unit will greatly aid the forthcoming removal and storage of the FDNPS debris.

CRediT authorship contribution statement

Ayumi Itoh: Writing – original draft, Visualization, Methodology, Investigation, Data curation, Conceptualization. **Masato Mizokami:** Writing – review & editing. **Mutsumi Hirai:** Writing – review & editing, Supervision.

Declaration of competing interest

The authors declare that they have no known competing financial interests or personal relationships that could have appeared to influence the work reported in this paper.

Supplementary materials

Supplementary material associated with this article can be found, in the online version, at doi:10.1016/j.jnucmat.2025.155892.

Data availability

Data will be made available on request.

References

[1] Tokyo Electric Power Co. Ltd., Sample analysis to understand the accident situation (Attachment 5), 2022. https://www.tepco.co.jp/en/hd/decommission/information/accident_unconfirmed/pdf/221110e0106.pdf (accessed May 4, 2024).

[2] A. Nakayoshi, T. Mitsugi, S. Sasaki, K. Maeda, Analysis of deposits inside the reactor at Fukushima Daiichi Nuclear Power Station (JAEA-Data/Code-2021-011), in: Japan Atomic Energy Agency, Ibaraki, 2021, https://doi.org/10.1148/jaea-data-code-2021-011.

[3] Ikeuchi, H.; Sasaki, S.; Onishi, T.; Nakayoshi, A.; Arai, Y.; Sato, T.; Ohgi, H.; Sekio, Y; Yamaguchi, Y.; Morishita, K.; Maeda, K., Analysis of deposits inside the reactor at fukushima daiichi nuclear power station (JAEA-Data/Code-2023-005), Japan Atomic Energy Agency, Ibaraki, 2023. doi:10.11484/jaea-data-code-2023-005.

[4] M. Kurata, N. Okuzumi, A. Nakayoshi, H. Ikeuchi, S. Koyama, Step-by-step challenge of debris characterization for the decommissioning of Fukushima-Daiichi Nuclear Power Station (FDNPS), J. Nucl. Sci. Technol. 59 (2022) 807–834, https://doi.org/10.1080/00223131.2022.2040393.

[5] H. Ohgi, Y. Nagae, M. Kurata, Thermodynamic evaluation on solidification path for U-Zr-Fe-O corium, in: Proceedings of the International Topical Workshop on Fukushima Decommissioning Research 2022, 2022, p. 1066, https://doi.org/10.1299/jsmefdr.2022.0_1066.

[6] B. Breeden, M. Poschmann, M.H.A. Piro, Using MELCOR with enhanced predictive capabilities via thermochimica to model two severe accident cases of a generic BWR with Zry-2 and FeCrAl, Nucl. Eng. Des. 419 (2024) 112957, https://doi.org/10.1016/J.NUCENGDES.2024.112957.

[7] C. Gueneau, N. Dupin, L. Kjellqvist, E. Geiger, M. Kurata, S. Goss, A. Quaini, R. Hania, A.L. Smith, M.H.A. Piro, T. Besmann, P.E.A. Turchi, J.C. Dumas, J. Welland, T. Ogata, B.O. Lee, J.R. Kennedy, C. Adkins, M. Bankhead, D. Costa, Calphad TAF-ID : an international thermodynamic database for nuclear fuels applications, Calphad 72 (2021) 102212, https://doi.org/10.1016/j.calphad.2020.102212.

[8] G.H. Gulliver, The quantitative effect of rapid cooling upon the constitution of binary alloys, J. Inst. Met 9 (1913) 120–157.

[9] Thermo-Calc software, Thermo-calc documentation Set, version 2024b (accessed 21 June 2024), (2024).

[10] P. Schaffnit, C. Stallybrass, J. Konrad, F. Stein, M. Weinberg, A Scheil–Gulliver model dedicated to the solidification of steel, Calphad 48 (2015) 184–188, https://doi.org/10.1016/j.calphad.2015.01.002.

[11] Thermo-Calc software, The TC-python API programmer guide 2024b (accessed 21 June 2024), (2024).

[12] P. Piluso, G. Trillon, C. Journeau, The UO2–ZrO2 system at high temperature (T >2000K): importance of the meta-stable phases under severe accident conditions, J. Nucl. Mater. 344 (2005) 259–264, https://doi.org/10.1016/j.jnucmat.2005.04.052.

[13] Trillon, G., Analysis of the corium phases by X-ray diffraction (CEA-R–6045), 2004.

[14] A. Brown, G.J. McIntyre, C. Gräslund, Analysis of crystalline phases in core bore materials from three mile island unit 2, Nucl. Technol. 87 (1989) 137–145, https://doi.org/10.13182/NT89-A27643.

[15] Geiger, E.; Benes, O.; Vigier, J.; Boboridis, K.; Robba, D.; Colle, J.; Cremer, B.; Ernstberger, M.; Poeml, P.; Himbert, J.; Gardeur, S.; Lajarge, P.; Popa, K.; Boshoven, C.; Vlahovic, L.; Wiss, T.; Piro, M.H.; Konings, R., Experimental validation of the TAF-ID: High temperature behaviour of simulated Ex-vessel corium and MOX-Lanthanides (Ce, Gd, La, Nd), Publications Office of the European Union, Luxembourg, 2023, doi:10.2760/693912.

[16] M. Takano, T. Nishi, N. Shirasu, Characterization of solidified melt among materials of UO2fuel and B4C control blade, J. Nucl. Sci. Technol. 51 (2014) 859–875, https://doi.org/10.1080/00223131.2014.912567.

[17] M. Steinbrück, Degradation and oxidation of B4C control rod segments at high temperatures, J. Nucl. Mater. 400 (2010) 138–150, https://doi.org/10.1016/j.jnucmat.2010.02.022.

[18] K. Inoue, A. Itoh, M. Mizokami, M. Hirai, Evaluation of boron evaporation kinetics from stainless-steel–B4C alloy during steam oxidation at high temperatures, J. Nucl. Mater. 603 (2025) 155456, https://doi.org/10.1016/j.jnucmat.2024.155456.

[19] B.J. Lewis, W.T. Thompson, F.C. Iglesias, 2.20-fission product chemistry in oxide fuels. Comprehensive Nuclear Materials, Elsevier, Amsterdam, 2012, pp. 515–546.

[20] Nishihara, K.; Iwamoto, H.; Suyama, K., Estimation of fuel compositions in Fukushima-Daiichi Nuclear Power Plant (JAEA-Data/Code-2012-018), Japan Atomic Energy Agency, Ibaraki, 2012, doi:10.11484/jaea-data-code-2012-018.